

A Case Study on Low-Cost Tip-Tilt Adaptive Optics Systems for
the Apache Point Observatory 3.5-m Telescope

Jee-Ho Kim

April 20, 2023

Advisor: Dr. John Wilson

Department of Astronomy
University of Virginia

This thesis is submitted in partial completion of the requirements of the BS Astronomy-Physics Major.

A Case Study on Low-Cost Tip-Tilt Adaptive Optics Systems for the Apache Point Observatory 3.5-m Telescope

Jee-Ho Kim¹ AND John Wilson¹

¹*Department of Astronomy, University of Virginia, Charlottesville, VA, 22904, USA*

ABSTRACT

A new echelle spectrograph is proposed for the 3.5-m telescope at Apache Point Observatory (APO), part of an effort to replace aging instrumentation and ensure its longevity. To further improve the capabilities of the instrument, we investigate the benefits of commissioning a low-cost adaptive optics system correcting low-order aberrations, namely tip-tilt. We compare two methods of correcting tip-tilt: centroid tracking and peak tracking. Centroid tracking follows the image's first order moment, and peak tracking, also known as shift-and-add (SAA), follows the brightest peak in an image. Tracking algorithms are developed and applied to high speed images from APO to determine their levels of improvement in terms of enslitted energy as a function of slit width. We found centroid tracking consistently performs better, at a maximum increase of at least 2%. The located centroids were also converted into a measurement of vibrational power, indicating overall wind speeds of 5–7 m/s above APO.

Keywords: adaptive optics — tip-tilt — centroids — shift-and-add

1. INTRODUCTION

Four-meter class telescopes are crucial to the scientific ecosystem, conducting follow-up observations of targets singled out from missions like TESS and the upcoming Vera C. Rubin Observatory. The Apache Point Observatory 3.5-m telescope has demonstrated its capabilities in continuing measurements of TESS candidate planets (Beard et al. 2022; Stefansson et al. 2018). To that effect, a new echelle spectrograph is currently being proposed to replace the twenty-year-old Astrophysical Research Consortium (ARC) Echelle Spectrograph. The effectiveness of the spectrograph could be augmented with the addition of tip-tilt image stabilization. Major limitations in image quality come from atmospheric turbulence, which bends light towards the telescope at different angles due to the varying indices of refraction of turbulent cells, and the mechanical jitter of the telescope itself. These low-order aberrations, modeled as low Zernike modes, cause the greatest variance in wavefront surfaces (Fried 1966). Effectively, imprecision in target location on the field of view increases, spreading out light and decreasing image quality. Adaptive optics

(AO) allows for these effects to be corrected in real time with the help of wavefront sensors analyzing approach- ing light. APO currently has no AO system in place.

Tip-tilt corrects the first two low Zernike modes. This type of AO system requires only a high-speed CCD camera, a tip-tilt mirror, and control software. A high-speed camera is needed to account for the rapid changes in atmosphere. The frequency of turbulent variations typically range from 20–40 Hz (Fried 1990). Consequently, near instantaneous specklegrams must be taken with a tip-tilt system to fully address atmospheric effects. If the exposure time is too long, the distortions average out and the image appears blurrier.

Centroid tracking and peak tracking, or real-time shift-and-add (SAA), are both algorithms for tip-tilt corrections. Centroid tracking adjusts the mirror according to the motion of the centroid, the image's first-order moment. Alternatively, tip-tilt with SAA operates by shifting the brightest speckles in a series of images on top of each other and adding them up. SAA improves image quality with worsening seeing, although its algorithm is more difficult to develop. It originated from efforts to improve the spatial resolution of optical telescopes and was initially proposed as a post-processing technique (Lynds et al. 1976; Bates & Cady 1980; Bates & Fright 1982). Both centroid and peak tracking can use fainter guide stars and can operate with a larger field of

view than more complex, higher-order corrections (Glin-demann 1997).

Tip-tilt systems have been implemented at other 4-m class telescopes with improved observations. Such systems include the Camera High Angular Resolution Module (CHARM) at the Calar Alto 3.5-m telescope (Glin-demann et al. 1997), the tip-tilt secondary mirror installed at the NOAO Blanco 4-m telescope (Perez & Elston 1998), and the NN-explore Exoplanet Investigations with Doppler spectroscopy (NEID) Port Adapter’s system at the 3.5-m Wisconsin Indiana Yale NOAO (WIYN) telescope (Li et al. 2022).

Crucial to note, however, is that foundational literature and current work commonly quantify the efficiency of an AO system by its improvement in Strehl ratio, which correlates better performance with a narrower FWHM (Roddier 1990; Roddier et al. 1991; Roddier 1998; Racine 2006). The Strehl ratio is defined as the ratio between the maximum intensity of an observed point source to the maximum intensity of the diffraction-limited image.

Our motivation for this work is to maximize the potential return from the proposed echelle spectrograph. Regarding spectrographs, we need to instead focus on improvements in enslitted energy rather than Strehl ratio. In fact, Jenkins (1998) found that the largest gain in FWHM results in the smallest amount of energy encircled within that FWHM. A narrower slit improves the resolution of the spectrograph and increases radial velocity precision diminished by the slit effect — the phenomenon where slit displacements about the source center induces wavelength errors. The major drawback of reducing slit width is loss of light, however, meaning loss of information (Bacon et al. 1995). Thus, increasing the energy of the source contained in a slit can create the best balance between instrument sensitivity and light retention. Tip-tilt tracking can accomplish this by centering a source within the slit in real-time and minimizing wasted light.

We conduct a comparative investigation into peak tracking versus centroid tracking in expectation of proposing an optimal low-cost, off-the-shelf AO addition to correct low Zernike mode aberrations in the fore optics of the new spectrograph. We include studies on the vibrational power affecting the telescope as well, contextualizing it as a source of tip-tilt error. This paper is outlined as follows: Section 2 details the APO data used in this study; Section 3 provides the methodology for analysis carried out on the data, including tracking algorithms; Section 4 shows the results of our work; Section 5 appraises the potential of our findings in im-

proving spectrograph resolution and charts next steps; and Section 6 summarizes our main takeaways.

2. DATA

We examined specklegrams taken using the APO 3.5-m telescope with the visiting Differential Speckle Survey Instrument (Horch et al. 2009). The DSSI employs two Electron Multiplying Charge-Coupled Devices (EMCCDs). The EMCCDs are the iXon Ultra 888 model from Andor. We hereon refer to each detector as camera 1 and camera 2. Camera 1 has a 692 nm filter with a 40 nm FWHM, and camera 2 has an 880 nm filter with a 50 nm FWHM. The frames from these cameras are both set so that the positive y-direction points northward on the sky. For camera 1, the x-axis points eastward, and for camera 2, the x-axis points westward. Consequently, all the 880 nm data has been flipped to align with the 692 nm coordinate system.

Although camera 2 has a non-uniform plate scale due to its dichroic, we assume its approximate overall plate scale is 0.0225 arcsec/pixel, the plate scale of camera 1.

The first data run occurred in May 2022. The first set of data tracked the centroid centers of a target for low (~ 1) and high (~ 2) airmass cases using both cameras. 1000 frames were taken at a sampling frequency of 11.9 Hz, though we only have the calculated centroid center deviations in x and y and not the actual images. This data set is hereafter called the airmass data. For all data, frames are 256×256 pixels with a 1×1 binning. The second set of data included the entire FITS cube. Both filters were used to take specklegrams of two targets, here labeled A and B. The same sampling frequency and sample size comprise these data.

The second observation run took place in November 2022. Different settings were used to take these data, intended to explore a broader range of vibrational frequencies. Section 5.2 elaborates on this reasoning. The telescope was pointed into the wind at roughly 8 mph. Samples were taken over a longer period of time — 8191 frames at a higher rate of 41.7 Hz. Cameras 1 and 2 each examined two targets together, sources C and D.

All FITS cubes were first background subtracted. Assuming minimal contamination from the source in the bottom five rows of each frame, the median value within that span was subtracted on a frame-by-frame basis.

3. METHODS

First, we detail the algorithms used to conduct peak tracking and centroid tracking. From these two methods, we are able to produce a variety of analytical plots to characterize their performance on APO data.

For both tracking methods, each frame was first smoothed with a Gaussian kernel. This was done to

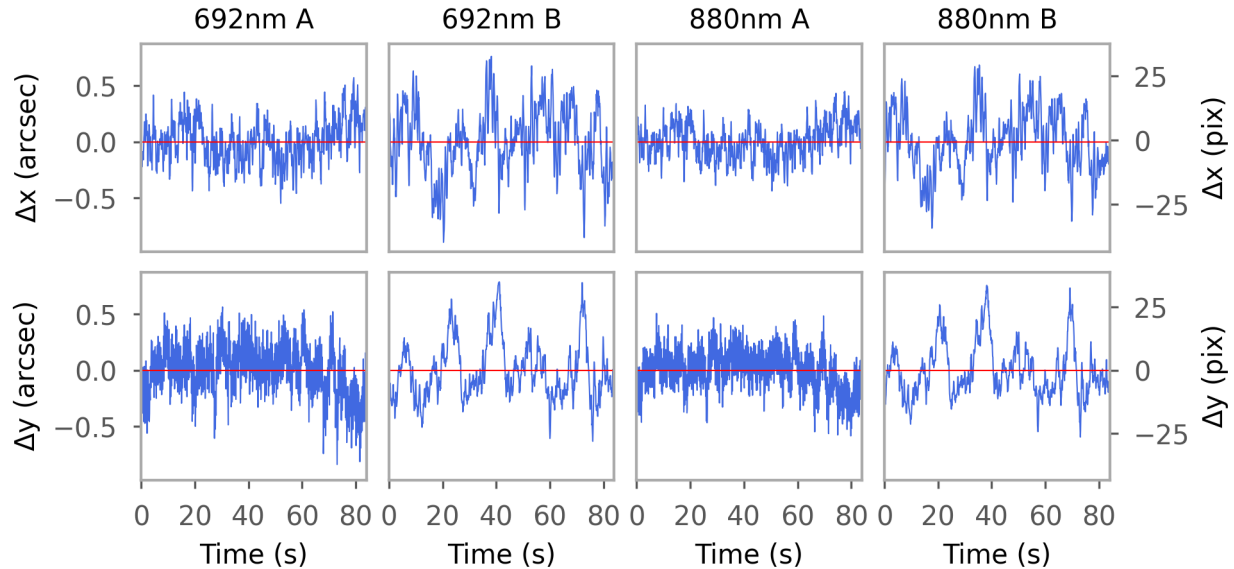


Figure 1. The deviation in centroid location for the A and B measurements in both wavelength filters. The variation is measured with respect to the mean centroid coordinates. The top row follows the x-coordinates, and the bottom row follows the y-coordinates. Both units of arcseconds and pixels are displayed.

mitigate the effects of extraneously brightened pixels, such as those caused by cosmic rays. For observations of sources A and B, a 3σ kernel was used. We applied a 4σ kernel to the observations of targets C and D to account for the increased noise in these data.

3.1. Peak Tracking

From each smoothed frame, the brightest pixel is determined, which we expect to correspond with the brightest peak. The original background-subtracted data is then “rolled” so that the peak coordinates are centered in every frame. Rolling the data moves elements shifted beyond the last position in an array to the first position, so the total number of counts is preserved. This is crucial for examining enslitted energy later.

Once the peaks have been centered, the images are summed along the temporal axis. Typically, peak tracking results in a narrow extreme surrounded by a raised pedestal of flux.

3.2. Centroid Tracking

Centroid tracking follows the same logic as peak tracking, with the center of each centroid centered in the frame. The centroid center is calculated here as a center of mass of the entire specklegram. We use the `centroid_com` function in the `photutils` package to carry out this work.

This type of method typically will not create as sharp of an image as peak tracking, though it avoids the

pedestal issue of a higher level of flux surrounding the center.

Centroid and peak tracking were carried out on data of sources A, B, C, and D.

3.3. Power Spectral Density

From the centroid coordinates, we could analyze the nature of vibrations affecting the 3.5-m telescope. We define the error as the deviation of each centroid center from the mean.

Splitting the error into x- and y-deviations, we calculate the power spectral density (PSD) along the north-south axis and east-west axis on the sky. The PSD is taken as the square of the absolute value of the Fourier Transformed error, all along the frequency axis. The Discrete Fourier Transform module in NumPy functions was used to accomplish these computations. We also find the power law slope for the high frequency and low frequency range of the x-axis PSD by applying SciPy’s `curve_fit` function. For the airmass data, we approximate the low range meeting the high range at 0.4 Hz. For the errors on the source A and B observations, the two ranges split around 0.6 Hz.

As another measurement of vibration, we include the median of the root of the PSD in discretized frequency bins. Examining the power in this manner allows us to more easily visualize which parts of the frequency range are more active.

PSD calculations were applied to the airmass data and data for targets A and B. Sources C and D are omitted

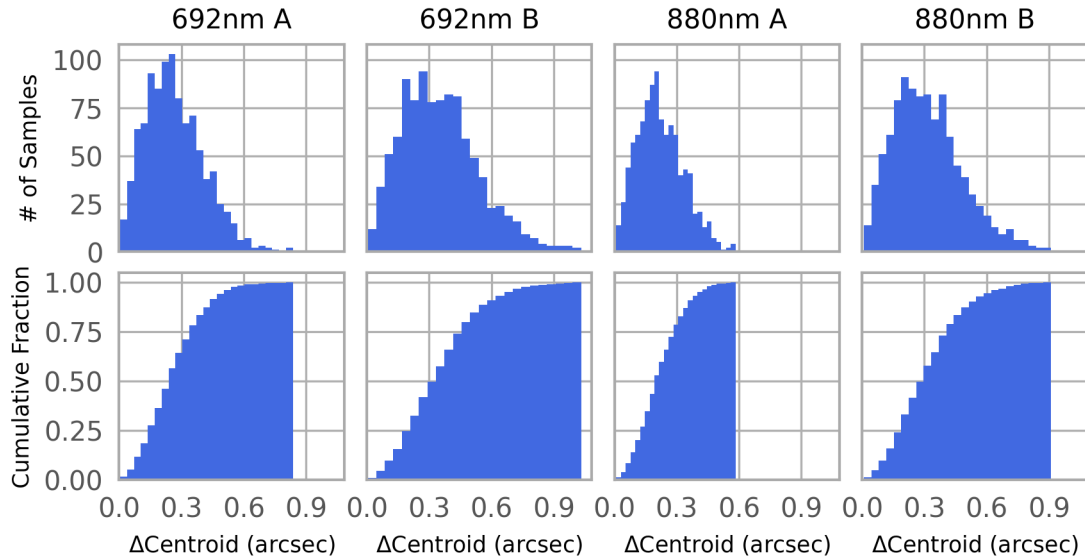


Figure 2. Centroid deviation plotted as a histogram (top) and a cumulative distribution function (bottom). The variation is measured as the radial distance to the mean centroid location.

from the main text of this paper for reasons outlined in Section 5.2.

3.4. Enslitted Energy

To compare peak tracking and centroid tracking in improving the resolution of an echelle spectrograph for the 3.5-m telescope, we examine the enslitted energy resulting from each method.

We first create profiles of the targets before and after applying a tip-tilt algorithm. The cubes of raw (background-subtracted) data, peak tracked data, and centroid tracked data are each summed into a single image, and then flattened along the north-south axis, resulting in a one-dimensional profile across the east-west direction. For analytical purposes, we then roll each profile so the peak of each profile is centered. From these profiles we can predict the improvements with varied slit widths.

We assume the echelle spectrograph slit is oriented north-south and centered on the peak of the source. In the case of an infinite slit, extending along the entirety of the y-axis, the enslitted energy is easier to calculate. For slit widths from 0 to 2 times the FWHM of the raw data’s profile, we sum all energy, or counts, within the slit for each data case and divide those values by the total energy. Thus, we get the enslitted energy normalized to the curve. The number of linear steps across the x-axis vary from 15 to 80 to remove artificial discretization effects and produce a smoothed line.

For the case of a finite slit, we assume a height of 3.2 arcseconds, the height of the most commonly used slit in APO’s current echelle spectrograph. Instead of

flattening the summed images along the entire vertical axis, we sum only the pixel rows spanning 1.6 arcseconds on either side of the image center. From this partial profile, we use the same technique to determine the enslitted energy over slit width. The total energy used here is the raw data’s summed counts over the rows spanning the slit height.

Enslitted energy investigations were carried out for the A, B, C, and D sets.

4. RESULTS

Here we provide our findings, beginning with the overview of vibrational power at the 3.5-m telescope. We then compare qualitatively and quantitatively the improvements from peak and centroid tracking.

4.1. Vibrational Analysis

4.1.1. Centroid Center Deviations

The x- and y-deviation in centroid centers over time is shown in Figure 1. The errors are calculated about the mean position of the centroid for sources A and B. Units of both arcseconds and pixels are included for convenience.

Minimal jitter is found in observations of source A, although the telescope appears to have had stronger movements when monitoring source B. Both DSSI cameras are seen to have experienced similar levels of vibration here.

These conclusions can be found more concisely in Figure 2, which has the corresponding histograms and cumulative distribution functions. The error here is the distance from the mean, or in other words, the radial

Name	Mean		RMS		Absolute Max Excursion	
	(pix)	(arcsec)	(pix)	(arcsec)	(pix)	(arcsec)
692nm A	-11.566	-0.260	8.284	0.186	25.286	0.569
	-35.303	-0.794	10.481	0.236	37.191	0.837
692nm B	16.477	0.371	13.382	0.301	39.649	0.892
	0.261	0.006	11.551	0.260	34.866	0.784
880nm A	11.110	0.250	6.903	0.155	19.884	0.447
	-1.620	-0.036	8.530	0.192	25.921	0.583
880nm B	-1.846	-0.042	11.941	0.269	34.113	0.768
	3.693	0.083	10.573	0.238	33.498	0.754
692nm low airmass	-	-	8.834	0.199	30.697	0.691
	-	-	7.599	0.171	19.802	0.446
692nm high airmass	-	-	12.498	0.281	36.922	0.831
	-	-	10.876	0.245	34.638	0.779
880nm low airmass	-	-	8.157	0.184	26.764	0.602
	-	-	7.088	0.159	20.442	0.460
880nm high airmass	-	-	11.576	0.260	33.575	0.755
	-	-	10.452	0.235	34.890	0.785

Table 1. Calculated statistics for the centroid variation. The first row for each named measurement lists the x-values, and the second row lists the y-values.

deviation. For all datasets, at least half of the centroids are within 0.3 arcseconds of each other. We also see that the histograms peak around 0.2 arcseconds and vary in maximum distance. This is best exemplified by the source A measurements, which shows the disparity more conspicuously than the previous Figure 1. The longest centroid distance in the 880 nm filter is around 0.6 arcseconds, whereas it is closer to 0.8 arcseconds in the 692 nm filter.

Table 1 lists centroid deviation statistics for specklegrams of sources A and B and the airmass data. The mean position, error about the mean, and absolute max excursion are included. The first row for each set contains x-values, and the second row y-values. The means are not available for the airmass data, as those centroid locations were already calculated about the mean. The max excursions and RMSs are typically higher in the high airmass case versus the low airmass case, consistent with expectations that a high airmass region will have more turbulence.

4.1.2. Power Spectral Density

PSD plots for sources A and B and the airmass data appear in Figures 3 and 4, respectively. Blue lines indicate x-axis measurements, and red dotted lines represent the y-axis. On the left-hand side of the figures, the power law slopes for the low and high frequency ranges are included.

A large spike in power is found around 3.5 Hz for the source A measurements in y, which may be indicative of periodic vibration of the telescope. In the airmass

data, a sudden increase in power is found across both filters and axes at 4.5 Hz. APO scientists noticed such a phenomenon before, but we are as of yet unsure of its origin.¹ The PSD decreases with frequency in both figures as expected, and most of the vibrations come from the lower frequency range.

Assuming Kolmogorov turbulence, power law slopes of -2/3 and -11/3 are expected for the low and high frequency regions, respectively (Conan et al. 1995). The low frequency slopes all hover around -2/3, except for the source B slopes. The high frequency slopes are flatter than predicted — the power drops off more gradually.

4.2. Tracking Comparison

Now we examine the results of peak tracking and centroid tracking. Figure 5 plots the locations of peaks and centroids for sources A and B. The overlap between the two are significant, but they are not perfect matches. This can best be exemplified in the 692 nm data for source A, where the centroid can be found to skew more westward than the peak.

Figures 6 and 7 display the summed images for the raw data, peak tracked data, and centroid tracked data for the 880 nm A and B sets. With peak tracking, the characteristic bright point is immediately apparent. A dimmer halo surrounds the center. Although the centroid image does not have as dramatic an effect as peak tracking, several observations can be made. Centroid

¹ B. Ketzeback, Personal Communication.

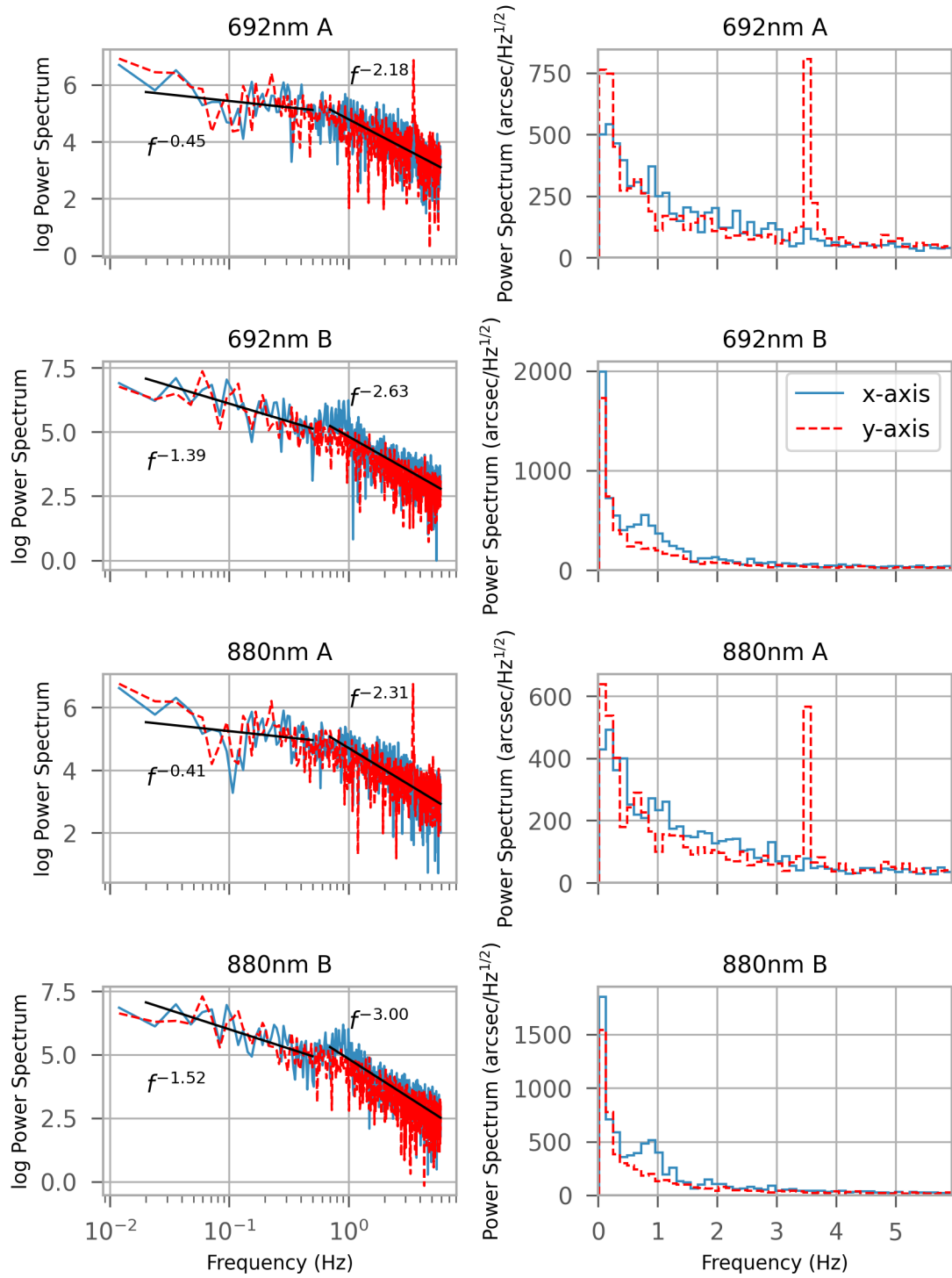


Figure 3. The power spectral density of the source A and source B measurements. The left side displays the PSD on a log scale, and the right side plots the median power vs. frequency. Linear fits on the x-axis data are shown on the left with their power law slopes.

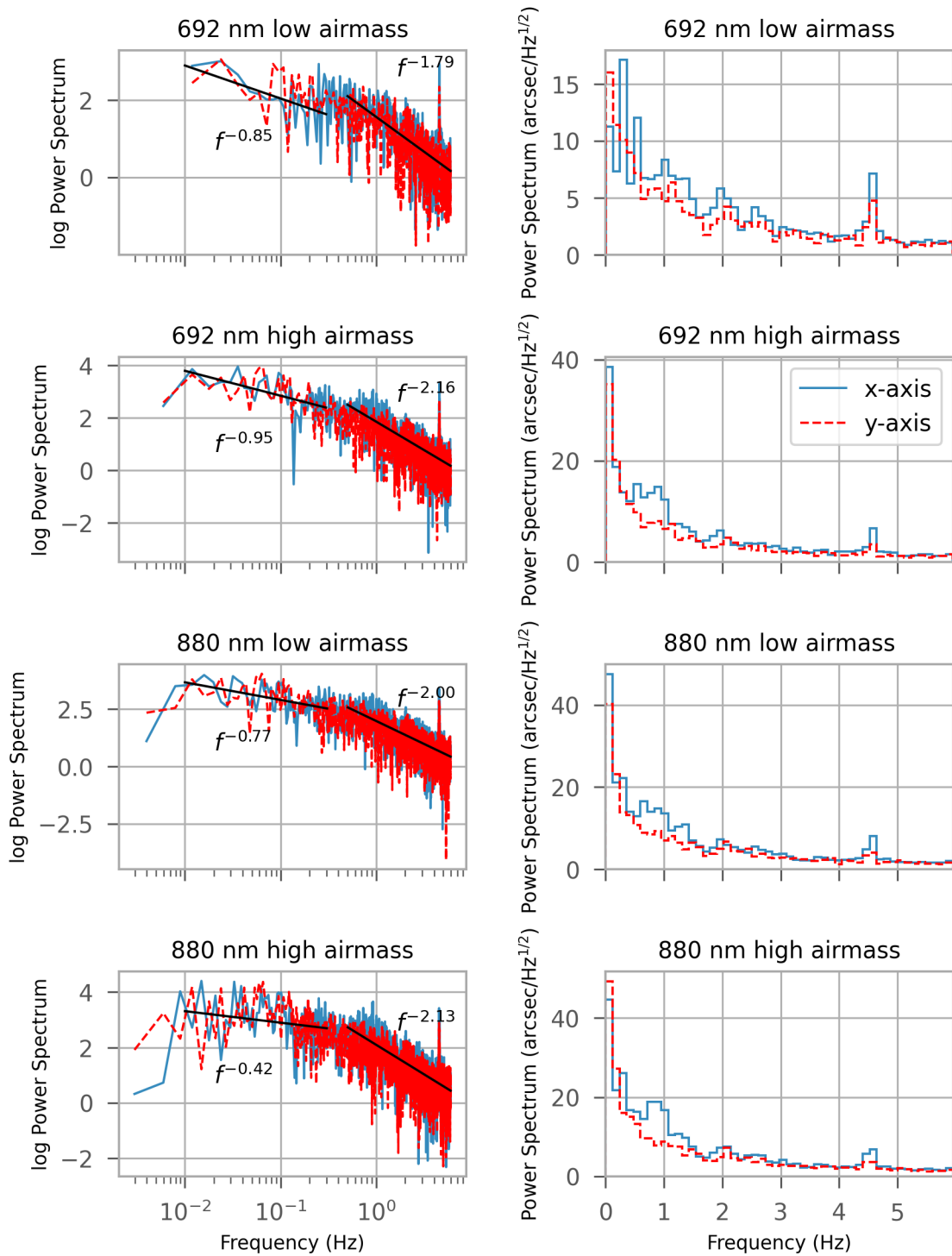


Figure 4. The power spectral density of the high and low airmass measurements. The left side displays the PSD on a log scale, and the right side plots the median power vs. frequency. Linear fits on the x-axis data are shown on the left with their power law slopes.

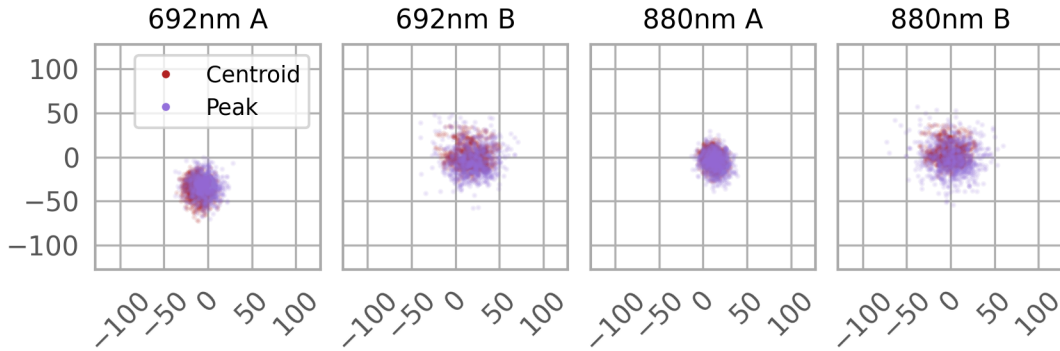


Figure 5. The locations of centroids and peaks, plotted together for comparison. Red markers indicate centroid centers, and purple markers denote peaks.

tracking can correct smeared images, like in the A image. The improvement in energy focus can also be seen by the difference in color bar range — the centroid image’s center is roughly a quarter brighter than the untouched case. Of course, peak tracking has the highest maximum, according to its nature of summing extrema.

4.3. Enslitted Energy Comparison

From full images in Figures 6 and 7, we flatten them down into profiles in Figures 8 and 9. The FWHM of the raw data is overplotted in red. Peak tracking consistently produces a brighter and narrower profile. Interestingly, the peak tracking curve can be seen to closely follow the raw data profile but deviate into a projected bump at the center. This phenomenon differs from our expectations of a dramatic spike in the center surrounded by a lower pedestal. The centroid tracking profiles tend to hold a consistent Gaussian shape, but narrower and taller than the raw data.

For the infinite slit case, there is tangible improvement in centroid tracking over peak tracking (Figures 10 and 11). The FWHM of the A data is 0.86 arcseconds, and 1.69 arcseconds for the B data. The vertical red line marks the $1.4 \times \text{FWHM}$ slit, which is the classical slit value (Bacon et al. 1995).

At that point for source A, the centroid tracking encompasses 1.2% more energy than peak tracking, and 2.4% more energy than the raw data. Greater improvements can be seen with a smaller slit width however, maximizing around 1 FWHM.

Source B shows smaller energy differences, with values from peak tracking and no tracking both being lower than centroid tracking by 0.02% at $1.4 \times \text{FWHM}$. Here, peak tracking actually tends to perform worse than no tracking towards larger slit widths. Again, centroid tracking optimizes at widths below the classical value.

The 3.2 arcsecond slit height shows slightly more improvement than the infinite scenario at larger slit widths

(Figures 12 and 13). Particularly with source B, the level of improvement for centroid tracking is constant for slit widths greater than one FWHM. At the classical value, centroid tracking enhances collected energy by 2.9% over peak tracking and 3.0% over the raw data. For target B in general, the peak tracking shows practically no difference with the raw data in terms of enslitted energy.

Analysis of other targets in Appendix A reveal agreeing trends.

5. DISCUSSION

Here we discuss the implications of our results on our understanding of atmospheric behavior at APO and the viability of an efficient tip-tilt system.

5.1. General Observations

In literature, peak tracking has often been advocated as a better algorithm than centroid tracking due to its ability to better improve the Strehl ratio (Christou 1991; Tokovinin et al. 2010). This work expands on a less considered aspect of tip-tilt application, which is its effect on enslitted energy improvements. We found centroid tracking performs better than peak tracking in this case. The implications of this bode well for implementation, as centroid tracking algorithms are more established in the field and easier to incorporate.

The centroid tracking has been shown to increase the enslitted energy by at least 2% compared to no tracking. Though not a large enhancement, this could have been predicted by the 3.5-m telescope’s characteristic number of speckles, which is on the order of $(D/r_0)^2$ (Roddier et al. 1991). r_0 is the Fried’s parameter, which is the size of turbulent cells in the atmosphere. D is the diameter of the telescope. Assuming a cell size of 10 cm, $D/r_0 = 35$. With so many speckles expected while imaging, we can follow the logic that it is harder to make significant advancements in energy concentration. Our

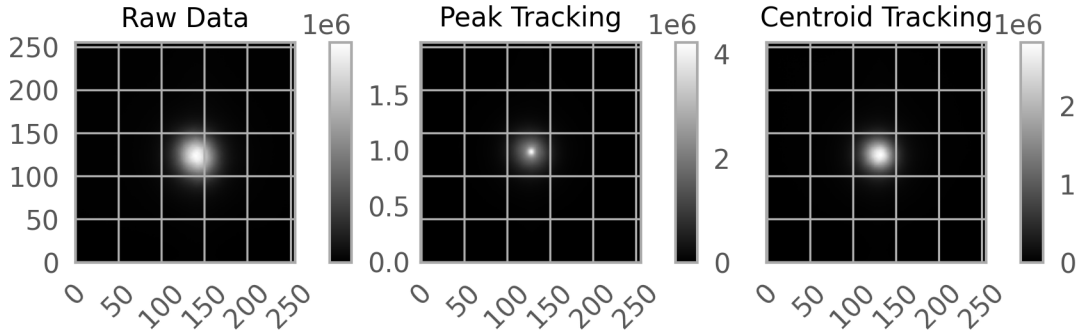


Figure 6. Summed images for the 880 nm A measurements. From left to right, each frame shows the effect of no tracking, peak tracking, and centroid tracking. In the latter two cases, the peaks and centroids have been centered and then added together.

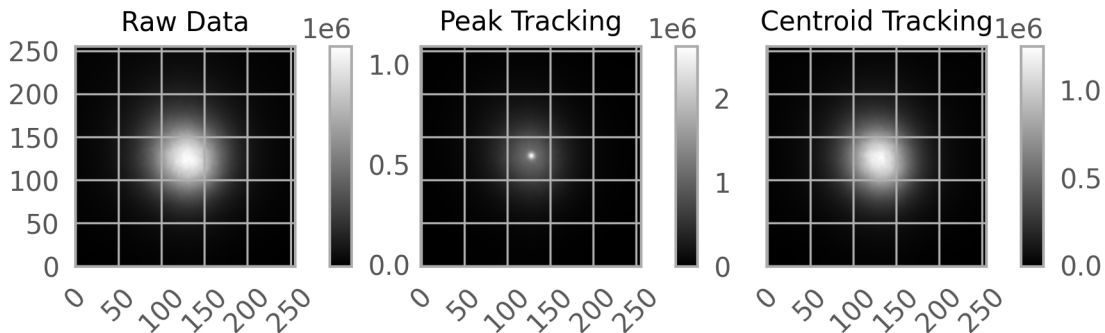


Figure 7. Summed images for the 880 nm B measurements. From left to right, each frame shows the effect of no tracking, peak tracking, and centroid tracking. In the latter two cases, the peaks and centroids have been centered and then added together.

methods of fixating on a single centroid center or bright speckle cannot gather together the energy dispersed over so many sub-regions. In addition, the seeing-limited angular resolution is approximately $\lambda/r_0 = 1.43$ arcseconds, assuming a wavelength of 692 nm. To begin with, this is not much larger than the telescope’s FWHM of 1.2 arcseconds.

Christou (1991) also found that centroid tracking consistently has a higher percentage of encircled energy than peak tracking, on a comparable order of one percentage. The difference between two methods increases with D/r_0 .

For a Shack-Hartmann wavefront sensor, the relationship between the transient frequency and wind speed is

$$f_t = 0.3v/D \quad (1)$$

for ideal power law slopes of $-2/3$ and $-11/3$ under the Kolmogorov model. This equation assumes a homogeneous turbulent layer in the atmosphere, where wind speed is independent of altitude (Conan et al. 1995). f_t , the transient frequency, is the point of separation between the low-frequency and high-frequency regimes of the power spectrum (Glindemann 1997). Low frequencies are dominated by tip-tilt aberrations, and once

corrected, should increase the power law slope to $4/3$. The size of subapertures tends to set the behavior at high frequencies (Greenwood & Fried 1976).

The low-frequency slopes, noted in Figures 3 and 4, generally agree with the Kolmogorov values, except for source B. We do not find as strong an alignment with the high-frequency power law. The Kolmogorov approximation generally works best in the lower frequency range, so these results are not unexpected. At the 3.5-m WIYN telescope, their PSD plots also only held consistent for that range (Claver et al. 1998).

If we apply Equation 1 to roughly approximate the effective wind speed at APO, we find speeds ranging from 5 m/s to 7 m/s. Under the Kolmogorov model, these values are interpreted as the average over all heights above the telescope. This is using $f_t = 0.4$ Hz and $f_t = 0.6$ Hz for the A/B observations and airmass studies, respectively. These values are slightly lower than the commonly assumed speed of 10 m/s.

The pedestal expected to be seen with peak tracking ended up appearing merged with the shape of the untracked profile. The sharply extending peak was only apparent in some cases, and with a short height above the pedestal. We attribute this diminished effect to the

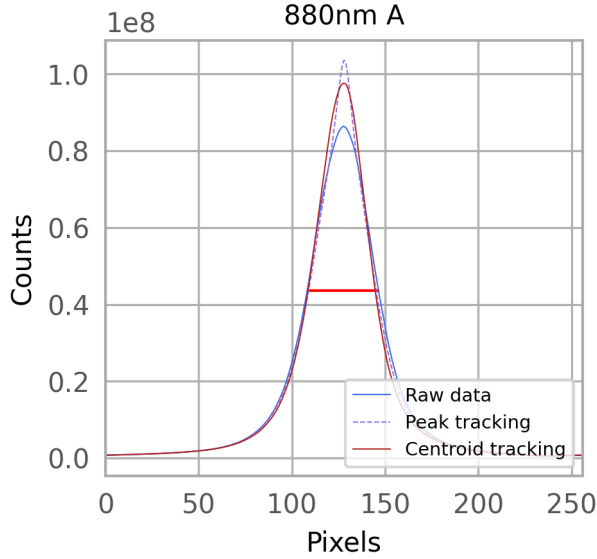


Figure 8. Profiles for the 880 nm source A analysis. The profiles were created by flattening down the vertical axis. The FWHM of the raw (untracked) data is shown in red.

relatively low sampling frequency of the data. From Tyler (1994), we estimate the Greenwood frequency — the frequency at which the images are distorted by atmospheric turbulence and at which AO systems should optimally operate — as nine times the fundamental tracking bandwidth f_{TB} . Following the simplified f_{TB} relation from Glindemann (1997),

$$f_{TB} = 1.62v/D. \quad (2)$$

With our highest derived wind speed of $v = 7$ m/s, we find a tracking bandwidth of 3.24 Hz and a Greenwood frequency of ~ 30 Hz, much higher than our 11.9 Hz sampling frequency. Corroborating this supposition is the work of Voitsekhovich & Orlov (2015), who found similar results for frequencies < 50 Hz. In order to create a more dramatic peak, specklegrams must be taken at a faster cadence.

One other factor that could have impacted accuracy was the fact that the focus was not the same between cameras 1 and 2. Optimal focus is needed for accurate specklegram measurements, but for the DSSI, where data are analyzed in the Fourier plane, the focus is less important.

5.2. Extended Runs

We requested data collection for the most recent November 2022 run so that the PSD could probe a more expansive frequency range. We chose a faster sampling rate to observe the vibrational power above 20 Hz. If the source moves too much during an exposure, that high-frequency agitation will not be accounted for, and the

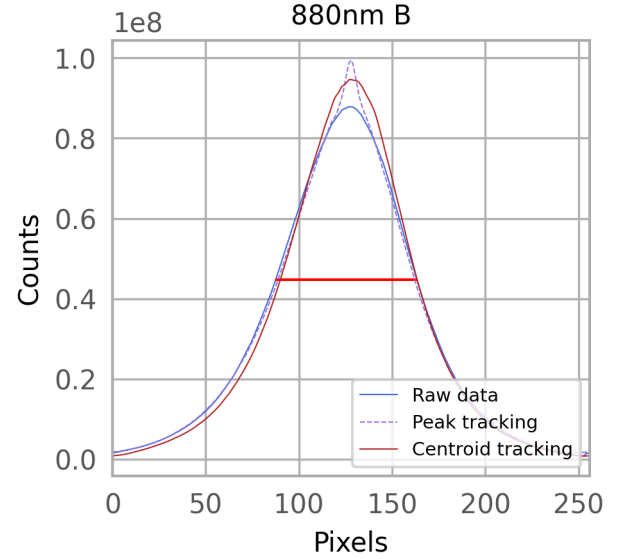


Figure 9. Profiles for the 880 nm source B analysis. The profiles were created by flattening down the vertical axis. The FWHM of the raw (untracked) data is shown in red.

measured change in position will be lower than the actual value (Martin 1987). Wind speed is one factor that can lead to this effect. On the other end of the frequency range, the specklegrams were taken over a longer period of time to sample lower frequencies. An observing run of > 10 min would be ideal to probe this region (Glindemann 1997), but due to variable weather conditions, the sets only cover ~ 200 seconds at a time.

We conducted the same analysis for these measurements of sources C and D as we did for sources A and B, but we encountered several issues while applying the tracking methods. Most likely due to the wind facing the telescope and the higher sampling frequency, many frames had too much noise to distinguish speckles. The centroid tracking algorithm in particular had difficulty locating a target on these data. The resulting plots are shown in Appendix B.

The peaks determined by the algorithm are much more consolidated than the centroids for these sets, though several peaks have been found on the outskirts of the frame due to noise (Figure 18). The centroid centers are scattered around the frames, and clearly do not probe the actual location of the sources. We find agreement with studies that the brightest spots tend to be distanced from the image centers (Christou 1991).

Although the summed images appear to show improvements with tracking, as seen in Figure 19, and especially in the case of peak tracking, their profiles reveal that these results are not reliable (Figure 20). The edges of the profiles do not approach 0 as expected, but

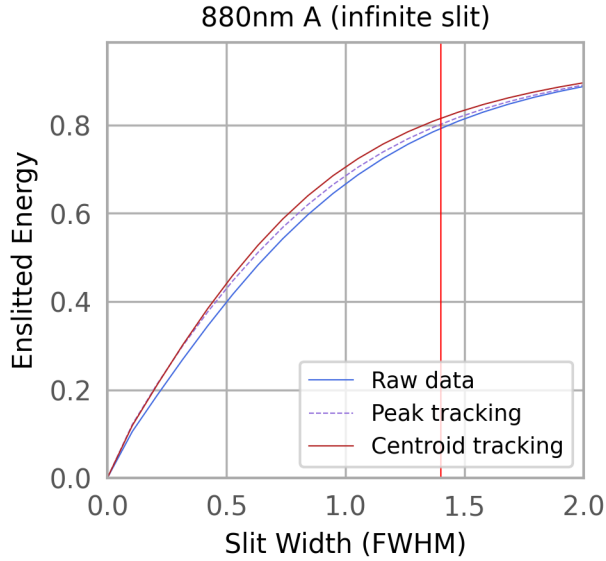


Figure 10. The enslitted energy, as a fraction of the total energy, within a range of slit widths from 0 to 2 times the FWHM of the raw data. The slit is assumed to extend infinitely along the vertical axis. The red vertical line marks $1.4 \times \text{FWHM}$, the classical slit width.

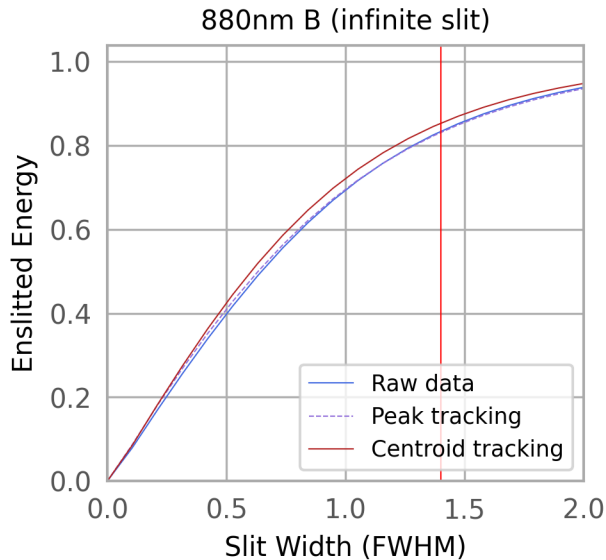


Figure 11. The enslitted energy, as a fraction of the total energy, within a range of slit widths from 0 to 2 times the FWHM of the raw data. The slit is assumed to extend infinitely along the vertical axis. The red vertical line marks $1.4 \times \text{FWHM}$, the classical slit width.

instead reach negative counts. As a result, the enslitted energy plots falsely conclude that peak tracking and centroid tracking add energy — they rapidly exceed 100% (Figures 21 and 22).

5.3. Future Work

Our work is just beginning on exploring the efficacy of a low-cost AO system for the new spectrograph. We plan on installing accelerometers at strategic points around the telescope to experimentally determine the mechanical jitter. Once we understand this type of vibration, we can easily separate out the atmospheric effects, and determine a more accurate transient frequency and wind speed. This same type of study was carried out at the Daniel K. Inouye Solar Telescope (DKIST) several years ago (McBride & McBride 2016; McBride & Stratton 2018). In the 90s, the non-atmospheric jitter on the APO 3.5-m telescope was determined to have an rms of 0.04 arcseconds, or 0.1 arcsecond FWHM (Kibblewhite et al. 1998). We hope to update that value now.

Improving the tracking algorithms so we can properly apply them to the recently acquired data is another key step to take. For example, the tip-tilt system used in the NN-explora Exoplanet Investigations with Doppler spectroscopy (NEID) Port Adapter at WIYN uses a 2D cross-correlation function to locate centroids. The center of mass function is employed only as a backup method for cases of poorer seeing (Li et al. 2022).

Lastly, more data will be taken with the DSSI with frame rates and set durations optimized for our purposes.

6. CONCLUSIONS

In preparation for proposing a low-cost tip-tilt system at the APO 3.5-m telescope, we characterized the current performance of the telescope and predicted improvements due to centroid and peak tracking. Supporting this endeavor, we also examined the vibrational power affecting the image jitter. We summarize our findings as follows:

- Centroid tracking consistently had greater improvements in enslitted energy compared to peak tracking and no tracking. A maximum enhancement of at least 2% can be derived.
- Our peak tracking algorithm is more apt in locating the image in poor seeing than our center of mass-based centroid tracking algorithm. A refinement of the tracking algorithm is recommended for further research.
- The Kolmogorov model for turbulence holds in the lower frequency (< 1 Hz) regime. The power law values we determine for the high frequency range has a lower magnitude than predicted.
- We approximated effective average wind speeds over APO in the range of 5–7 m/s.

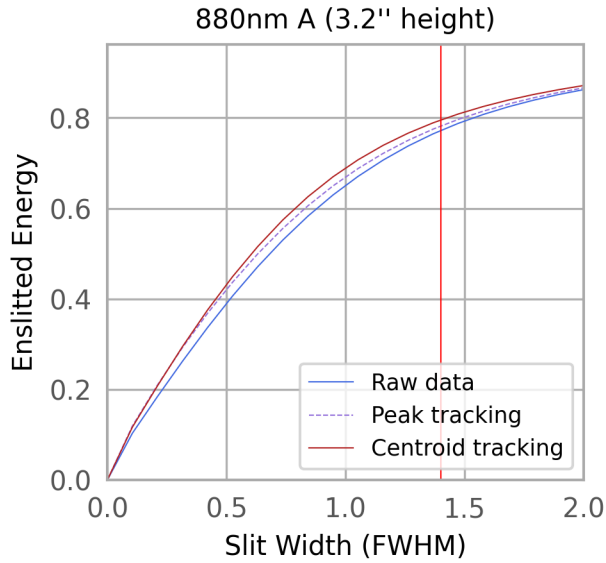


Figure 12. The enslitted energy, as a fraction of the total energy, within a range of slit widths from 0 to 2 times the FWHM of the raw data. The slit has a height of 3.2 arcseconds. The red vertical line marks $1.4 \times \text{FWHM}$, the classical slit width.

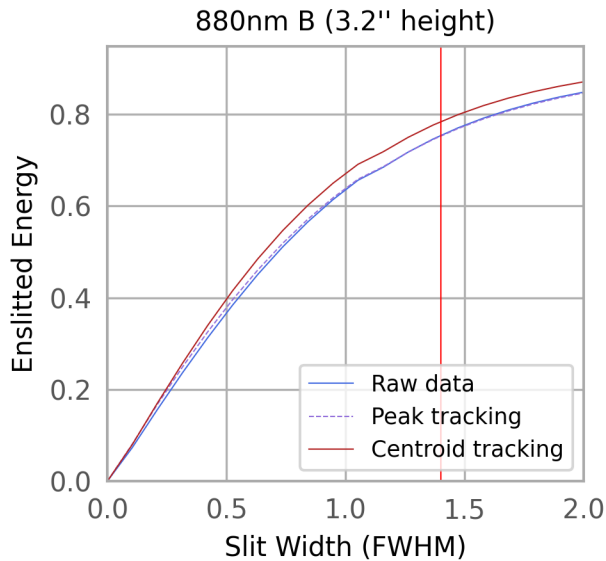


Figure 13. The enslitted energy, as a fraction of the total energy, within a range of slit widths from 0 to 2 times the FWHM of the raw data. The slit has a height of 3.2 arcseconds. The red vertical line marks $1.4 \times \text{FWHM}$, the classical slit width.

ACKNOWLEDGMENTS

We thank Jimmy Davidson and the DSSI Team for APO observations. J-H Kim thanks the UVA Astronomy fourth year undergraduates (Cole Faggert, Jillian Maxson, Ethan McKeever, Theo O’Neill, Louis Seyfritz, Sarah Shriner, Mint Tositrakul) for their support and friendship. J-H Kim thanks John Wilson for being a wonderful thesis advisor. This research made use of Photutils, an Astropy package for detection and photometry of astronomical sources (Bradley et al. 2022).

Facilities: APO

Software: Astropy (Astropy Collaboration et al. 2013), SciPy (Virtanen et al. 2020), Photutils (Bradley et al. 2022)

APPENDIX

A. ADDITIONAL ANALYSIS ON SOURCE B

Here we show the results of carrying out centroid tracking and peak tracking on source B in the 692 nm filter. The same trends are visible in these plots, but the improvement in enslitted energy is less. Figure 14 shows the summed images for the tracked and untracked cases. Fig 15 plots the profiles along the horizontal axis derived from the previous figure. The enslitted energy plots for the infinite slit and 3.2 arcsecond slit are found in Figures 16 and 17.

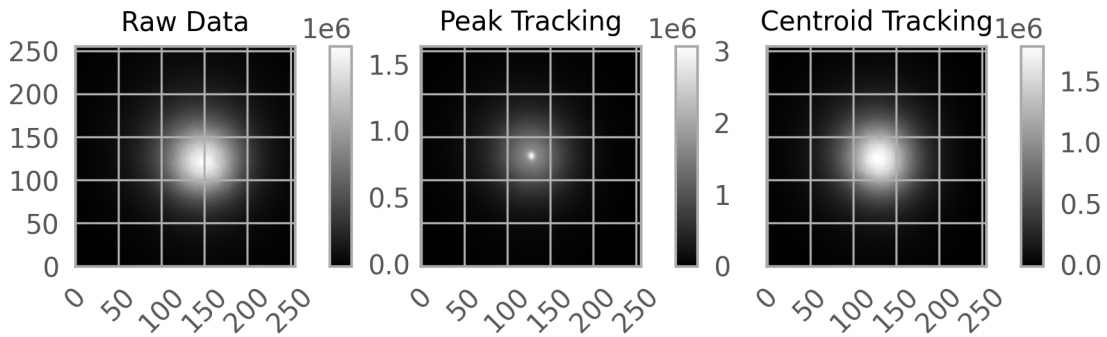


Figure 14. Summed images for the 692 nm B measurements. From left to right, each frame shows the effect of no tracking, peak tracking, and centroid tracking. In the latter two cases, the peaks and centroids have been centered and then added together.

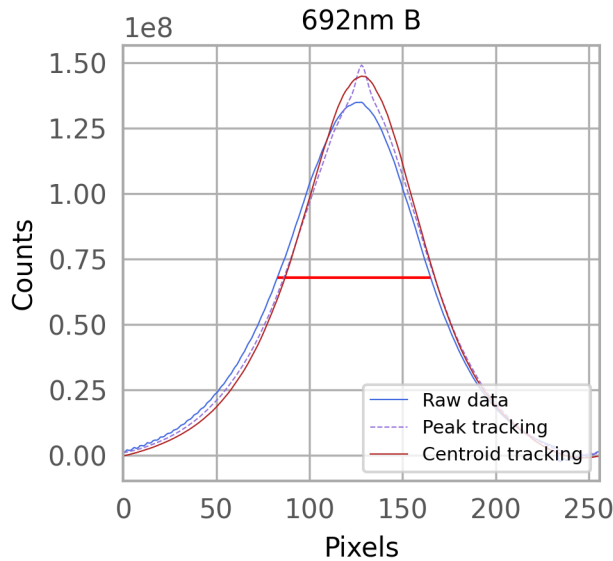


Figure 15. Profiles for the 692 nm source B analysis. The profiles were created by flattening down the vertical axis. The FWHM of the raw (untracked) data is shown in red.

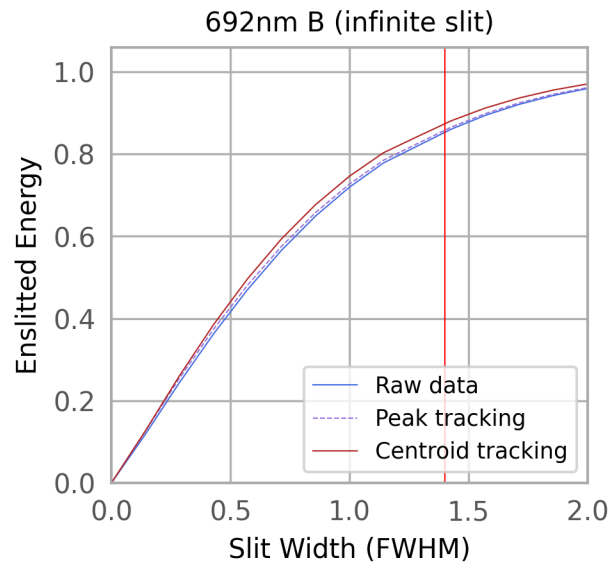


Figure 16. The enslitted energy, as a fraction of the total energy, within a range of slit widths from 0 to 2 times the FWHM of the raw data. The slit is assumed to extend infinitely along the vertical axis. The red vertical line marks $1.4 \times \text{FWHM}$, the classical slit width.

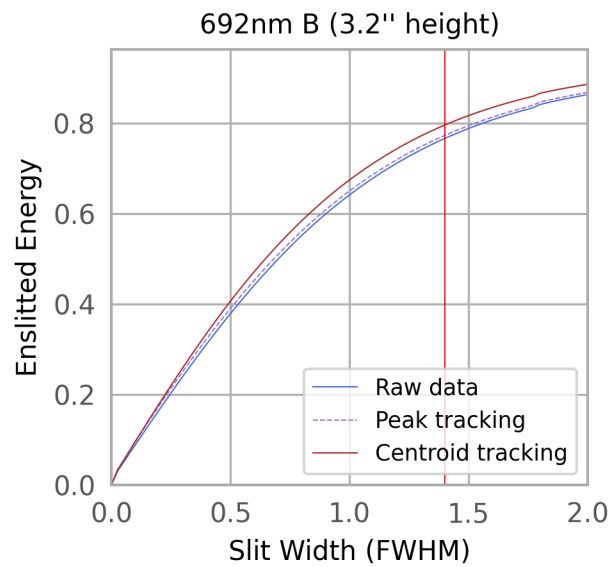


Figure 17. The enslitted energy, as a fraction of the total energy, within a range of slit widths from 0 to 2 times the FWHM of the raw data. The slit has a height of 3.2 arcseconds. The red vertical line marks $1.4 \times \text{FWHM}$, the classical slit width.

B. ADDITIONAL ANALYSIS ON SOURCE D

The results of applying the tracking algorithms to source D in the 880 nm filter are compiled here as an example of the errors that occurred when attempting to process the new data taken at a higher frequency with more frames. Figure 18 plots the centroids and peaks together. Both algorithms do not locate images with the same accuracy as with sources A and B — especially centroid tracking. The resulting summed images are shown in Figure 19. Their profiles are laid out in Figure 20, and the resulting enslitted energy plots can be found in Figures 21 and 22. Refer to Section 5.2 for elaboration on these data.

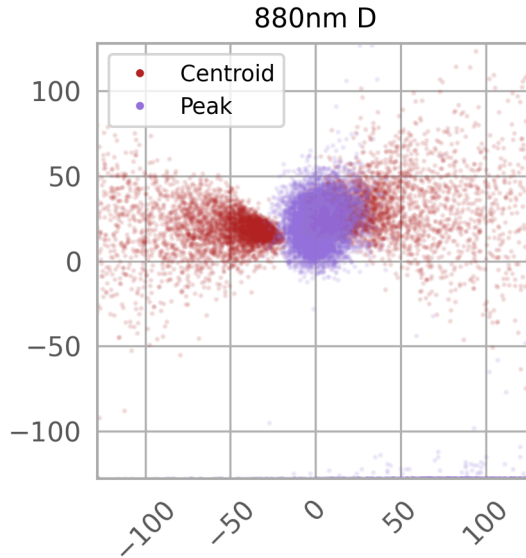


Figure 18. The locations of centroids and peaks, plotted together for comparison. Red markers indicate centroid centers, and purple markers denote peaks.

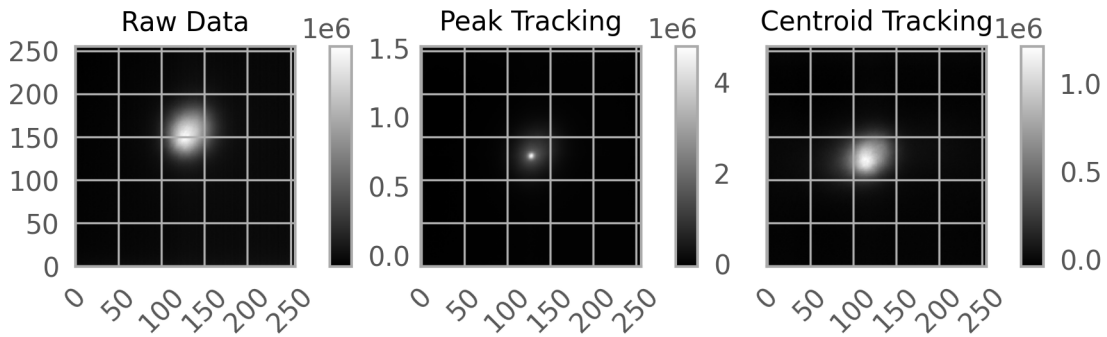


Figure 19. Summed images for the 880 nm D measurements. From left to right, each frame shows the effect of no tracking, peak tracking, and centroid tracking. In the latter two cases, the peaks and centroids have been centered and then added together.

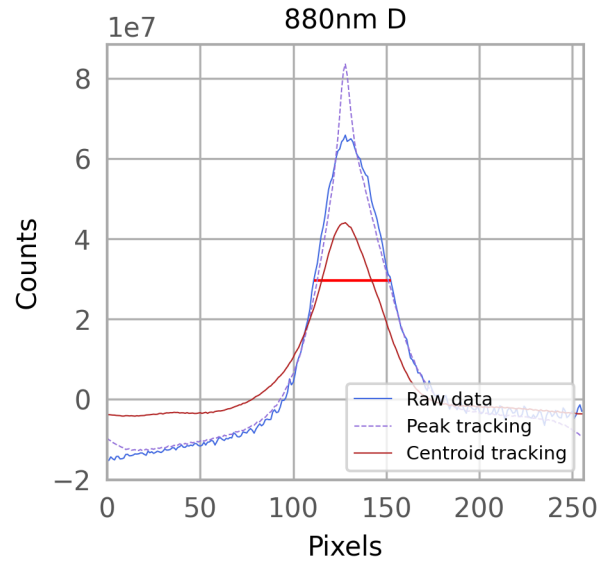


Figure 20. Profiles for the 880 nm source D analysis. The profiles were created by flattening down the vertical axis. The FWHM of the raw (untracked) data is shown in red.

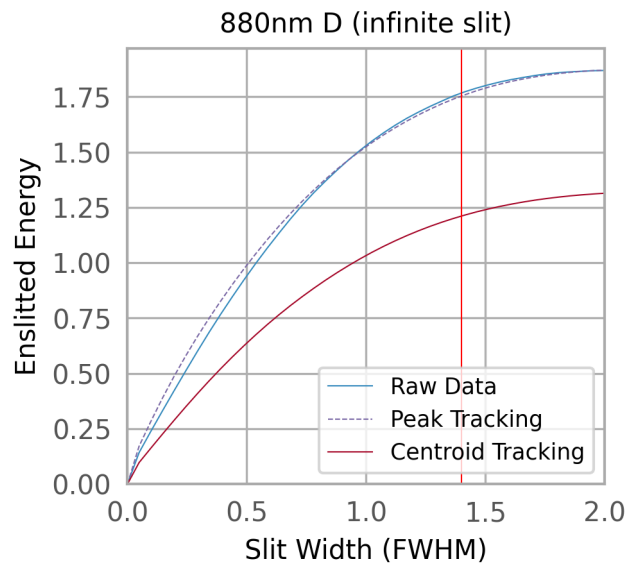


Figure 21. The enlitted energy, as a fraction of the total energy, within a range of slit widths from 0 to 2 times the FWHM of the raw data. The slit is assumed to extend infinitely along the vertical axis. The red vertical line marks $1.4 \times \text{FWHM}$, the classical slit width.

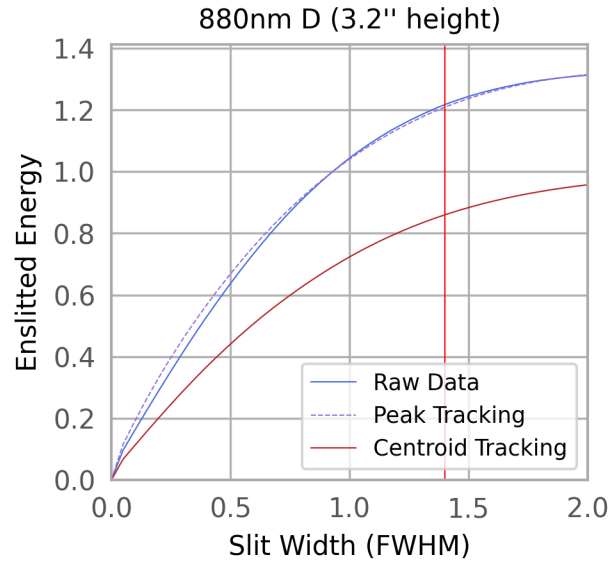


Figure 22. The enslitted energy, as a fraction of the total energy, within a range of slit widths from 0 to 2 times the FWHM of the raw data. The slit has a height of 3.2 arcseconds. The red vertical line marks $1.4 \times \text{FWHM}$, the classical slit width.

REFERENCES

- Astropy Collaboration, Robitaille, T. P., Tollerud, E. J., et al. 2013, *A&A*, 558, A33, doi: [10.1051/0004-6361/201322068](https://doi.org/10.1051/0004-6361/201322068)
- Bacon, R., Adam, G., Baranne, A., et al. 1995, *A&AS*, 113, 347
- Bates, R. H. T., & Cady, F. M. 1980, *Optics Communications*, 32, 365, doi: [10.1016/0030-4018\(80\)90261-8](https://doi.org/10.1016/0030-4018(80)90261-8)
- Bates, R. H. T., & Fright, W. R. 1982, *MNRAS*, 198, 1017, doi: [10.1093/mnras/198.4.1017](https://doi.org/10.1093/mnras/198.4.1017)
- Beard, C., Robertson, P., Kanodia, S., et al. 2022, *ApJ*, 936, 55, doi: [10.3847/1538-4357/ac8480](https://doi.org/10.3847/1538-4357/ac8480)
- Bradley, L., Sipőcz, B., Robitaille, T., et al. 2022, *astropy/photutils: 1.5.0*, 1.5.0, Zenodo, doi: [10.5281/zenodo.6825092](https://doi.org/10.5281/zenodo.6825092)
- Christou, J. C. 1991, *PASP*, 103, 1040, doi: [10.1086/132922](https://doi.org/10.1086/132922)
- Claver, C. F., Jacoby, G. H., Silva, D. R., & Code, A. D. 1998, in *Society of Photo-Optical Instrumentation Engineers (SPIE) Conference Series*, Vol. 3353, *Adaptive Optical System Technologies*, ed. D. Bonaccini & R. K. Tyson, 1130–1137, doi: [10.1117/12.321655](https://doi.org/10.1117/12.321655)
- Conan, J. M., Rousset, G., & Madec, P. Y. 1995, *Journal of the Optical Society of America A*, 12, 1559, doi: [10.1364/JOSAA.12.001559](https://doi.org/10.1364/JOSAA.12.001559)
- Fried, D. L. 1966, *Journal of the Optical Society of America (1917-1983)*, 56, 1372
- . 1990, *Journal of the Optical Society of America A*, 7, 946, doi: [10.1364/JOSAA.7.000946](https://doi.org/10.1364/JOSAA.7.000946)
- Glindemann, A. 1997, *PASP*, 109, 682, doi: [10.1086/133932](https://doi.org/10.1086/133932)
- Glindemann, A., McCaughrean, M. J., Hippler, S., et al. 1997, *PASP*, 109, 688, doi: [10.1086/133933](https://doi.org/10.1086/133933)
- Greenwood, D. P., & Fried, D. L. 1976, *Journal of the Optical Society of America (1917-1983)*, 66, 193
- Horch, E. P., Veillette, D. R., Baena Gallé, R., et al. 2009, *AJ*, 137, 5057, doi: [10.1088/0004-6256/137/6/5057](https://doi.org/10.1088/0004-6256/137/6/5057)
- Jenkins, C. R. 1998, *MNRAS*, 294, 69, doi: [10.1046/j.1365-8711.1998.01196.x](https://doi.org/10.1046/j.1365-8711.1998.01196.x)
- Kibblewhite, E. J., Chun, M. R., Larkin, J. E., et al. 1998, in *Society of Photo-Optical Instrumentation Engineers (SPIE) Conference Series*, Vol. 3353, *Adaptive Optical System Technologies*, ed. D. Bonaccini & R. K. Tyson, 60–71, doi: [10.1117/12.321726](https://doi.org/10.1117/12.321726)
- Li, D., Logsdon, S. E., McBride, W., et al. 2022, in *Society of Photo-Optical Instrumentation Engineers (SPIE) Conference Series*, Vol. 12184, *Ground-based and Airborne Instrumentation for Astronomy IX*, ed. C. J. Evans, J. J. Bryant, & K. Motohara, 121844O, doi: [10.1117/12.2629020](https://doi.org/10.1117/12.2629020)
- Lynds, C. R., Worden, S. P., & Harvey, J. W. 1976, *ApJ*, 207, 174, doi: [10.1086/154481](https://doi.org/10.1086/154481)
- Martin, H. M. 1987, *PASP*, 99, 1360, doi: [10.1086/132126](https://doi.org/10.1086/132126)

- McBride, W. R., & McBride, D. R. 2016, in Society of Photo-Optical Instrumentation Engineers (SPIE) Conference Series, Vol. 9911, Modeling, Systems Engineering, and Project Management for Astronomy VI, ed. G. Z. Angeli & P. Dierickx, 99112N, doi: [10.1117/12.2234096](https://doi.org/10.1117/12.2234096)
- McBride, W. R., & Stratton, M. 2018, in Society of Photo-Optical Instrumentation Engineers (SPIE) Conference Series, Vol. 10700, Ground-based and Airborne Telescopes VII, ed. H. K. Marshall & J. Spyromilio, 107000L, doi: [10.1117/12.2315038](https://doi.org/10.1117/12.2315038)
- Perez, G., & Elston, R. 1998, in Society of Photo-Optical Instrumentation Engineers (SPIE) Conference Series, Vol. 3352, Advanced Technology Optical/IR Telescopes VI, ed. L. M. Stepp, 328–333, doi: [10.1117/12.319320](https://doi.org/10.1117/12.319320)
- Racine, R. 2006, PASP, 118, 1066, doi: [10.1086/505990](https://doi.org/10.1086/505990)
- Roddier, F. 1998, PASP, 110, 837, doi: [10.1086/316194](https://doi.org/10.1086/316194)
- Roddier, F., Northcott, M., & Graves, J. E. 1991, PASP, 103, 131, doi: [10.1086/132802](https://doi.org/10.1086/132802)
- Roddier, N. 1990, Optical Engineering, 29, 1174, doi: [10.1117/12.55712](https://doi.org/10.1117/12.55712)
- Stefansson, G., Li, Y., Mahadevan, S., et al. 2018, AJ, 156, 266, doi: [10.3847/1538-3881/aae6ca](https://doi.org/10.3847/1538-3881/aae6ca)
- Tokovinin, A., Cantarutti, R., Tighe, R., et al. 2010, PASP, 122, 1483, doi: [10.1086/657903](https://doi.org/10.1086/657903)
- Tyler, G. A. 1994, Journal of the Optical Society of America A, 11, 358, doi: [10.1364/JOSAA.11.000358](https://doi.org/10.1364/JOSAA.11.000358)
- Virtanen, P., Gommers, R., Oliphant, T. E., et al. 2020, Nature Methods, 17, 261, doi: [10.1038/s41592-019-0686-2](https://doi.org/10.1038/s41592-019-0686-2)
- Voitsekhovich, V. V., & Orlov, V. G. 2015, PASP, 127, 795, doi: [10.1086/682401](https://doi.org/10.1086/682401)